UNIVERSITY *of* York

This is a repository copy of *The Structure of Tris(chloromethyl)amine in the Gas Phase Using Quantum Chemical Calculations and Gas Electron Diffraction and as a Solid and Melt using Raman Spectroscopy*.

White Rose
university consortium
Universities of Leeds, Sheffield & York

The Structure of Tris(chloromethyl)amine in the Gas Phase Using Quantum Chemical Calculations and Gas Electron Diffraction and as a Solid and Melt Using Raman Spectroscopy

Conor D. Rankine,[†] Sandra J. Atkinson,[‡] Mark R. Waterland,[§] Sarah L. Masters,[‡,*] and Derek A. Wann[†,*]

[†] Department of Chemistry, University of York, Heslington, York, U.K. YO10 5DD

[‡] School of Physical and Chemical Sciences, University of Canterbury, Private Bag 4800, Christchurch 8140, New Zealand

[§] Institute of Fundamental Sciences, Massey University, Private Bag 11 222, Palmerston North 4442, New Zealand

Corresponding Authors: sarah.masters@canterbury.ac.nz (S. L. M.); derek.wann@york.ac.uk (D.A.W.)

ABSTRACT: The equilibrium structure of tris(chloromethyl)amine, $N(CH_2Cl)_3$, has been determined in the gas phase using electron diffraction. Single-step distance corrections (representing the differences between the interatomic distances from the equilibrium structure and those from the vibrationally-averaged structure) and amplitudes of vibration have been computed using semi-empirical molecular dynamics (SE-MD) simulations in order to treat accurately the description of the low-frequency, large-amplitude vibrational modes associated particularly with one CH_2Cl group. A series of complementary theoretical calculations using the SOGGA11-X DFT functional with correlation-consistent basis sets of double, triple, and quadruple-ζ quality are also presented. The agreement between the experimental and theoretical equilibrium structural parameters attests to the accuracy of the applied theoretical calculations and of our gas-phase structural solution. Raman spectra have been recorded over a range of temperatures, allowing the solid and the melt to be studied, and the Raman-active intramolecular modes to be identified. Free from the influence of intermolecular interaction, the structure of tris(chloromethyl)amine in the gas phase is markedly different to that reported in the literature for the single crystal. This is discussed, and evidence for the anomeric effect in tris(chloromethyl)amine is evaluated.

KEYWORDS: gas-phase electron diffraction, gas-phase molecular structure, tris(chloromethyl)amine, Raman spectroscopy

■ INTRODUCTION

Tris(chloromethyl)amine, $N(CH_2Cl)_3$, (abbreviated TCMA) belongs to a family of tertiary amines that have non-typical near-planar geometries at their amine centers [1]. Members of this family have attracted the interest of the gas electron diffraction (GED) community before; the structure of tris(trifluoromethyl)amine, $N(CF_3)_3$, was established using GED in 1956 by Livingston and Vaughan [2] and was studied again with more modern techniques by Bürger, Niepel and Pawelke in 1979 [3]. The determination of the structure of tris(2,2,2-trifluoroethyl)amine, $N(CH_2CF_3)_3$, by Dimitrov *et al.* followed in 1994 [4]. For both species, the C–N–C′ angles about the amine center were determined to be close to 120° {$N(CF_3)_3$ C–N–C′ = 117.9(4)° [3]; $N(CH_2CF_3)_3$ C–N–C′ = 116.6(9)° [4]}, an observation that Klapötke *et al.* [1] have also made in their recent work on the synthesis and characterization *via* X-ray diffraction (XRD) of TCMA in the single crystal. A number of unique derivatives including tris(azidomethyl)amine, $N(CH_2N_3)_3$, and tris(5-nitrotetrazol-2-ylmethyl)amine, $N(CH_2[N_4CNO_2])_3$, were subsequently synthesized from TCMA and characterized by Klapötke *et al.* [1]. TCMA and tris(5-nitrotetrazol-2-ylmethyl)amine were determined to have similarly near-planar amide centers {TCMA C–N–C′ = 119.58(13)° [1]; $N(CH_2(N_4CNO_2))_3$ C–N–C′ = 119.81(13)° [1]} and a predisposition towards substitution at the CH_2 group which was found to be synthetically valuable [1]. In contrast, alkylated tertiary amines such as $N(CH_3)_3$ and $N(CH_2CH_3)_3$ typically have somewhat pyramidalized amine centers {$N(CH_3)_3$ C–N–C′ = 110.9(4)° [5]}. GED [5-9], spectroscopic [10-14], and dynamic NMR [15] studies targeting these species have been reported in the literature. The non-typical geometry of TCMA – which is not only defined by the near-planar amide center, but also by measureably shortened and lengthened N–C and C–Cl bonds {TCMA N–C = 140.9(4) pm, N–C′ = 141.1(2) pm, C–Cl = 184.1(3) pm, C′–Cl′ = 185.8(2) pm [1]}, respectively, and a wider-than-tetrahedral N–C–Cl angle {TCMA N–C–Cl = 114.57(19)°, N–C′–Cl′ = 114.35(16)° [1]} – is a manifestation of the generalized anomeric effect [16], which represents an extension of classic anomeric effect [17] beyond carbohydrate chemistry. The characteristic geometric consequences of the anomeric effect are particularly obvious in the absence of intermolecular interaction in the gas phase. Oberhammer *et al.* [18-25] have published prolifically on the subject and presented a number of theoretical calculations and high-quality structural solutions using GED, notably for $N(CH_3)_2(CH_2F)$ [19], $NX_2(CF_3)$ (where X is F [20], Cl [21], and Br [22]), $N(CH_3)(CF_3)_2$ [20], $(N(CF_3))_2$ [23,24], noting these geometric consequences in every case, and, more recently, for *N*-azidomethylpyrrolidine [25], although the strength of the anomeric effect, and consequently the extent to which they manifest, varies case-by-case. This work is summarized succinctly by Oberhammer in Ref. 18, to which readers are referred. One of the strongest anomeric effects has previously been predicted theoretically for $NH_2(CH_2F)$ [26-30], although it has yet to be observed in the gas phase on account of the instability of the species in question [18]. On paper, TCMA shares structural similarities with tris(2-chloroethyl)amine, $N(CH_2CH_2Cl)_3$, a powerful military-grade blister agent associated with acute cytotoxicity [31-34], but on the basis of the work by Oberhammer *et al.* [18-25], the three-dimensional geometry around the amide centre should be anticipated to be quite different. Indeed, the structural solution in the gas phase from GED may be anticipated to be quite different to that obtained for the single crystal using XRD, as work by Mitzel *et al.* [35-39] has demonstrated.

■ EXPERIMENTAL SECTION

Synthetic Procedure. A tenfold-reduced-scale synthesis of TCMA was carried out according to the synthetic procedure outlined by Fluck and Meiser [40]. TCMA was characterized by both ^{1}H and ^{13}C NMR spectroscopy.

Theoretical Calculations & Semi-Empirical Molecular Dynamics (SE-MD). All theoretical calculations were carried out using the Gaussian09 Rev. D01 software suite [41], while all SE-MD simulations were carried out using the CP2K MD code [42]. The computational resources required for the former were provided by the York Advanced Research Computing Cluster [43]; those required for the latter were provided by the UK National Service for Computational Chemistry Software (NSCCS) [44]. The nuclear labelling scheme referred to throughout this article is outlined in Fig. 1.
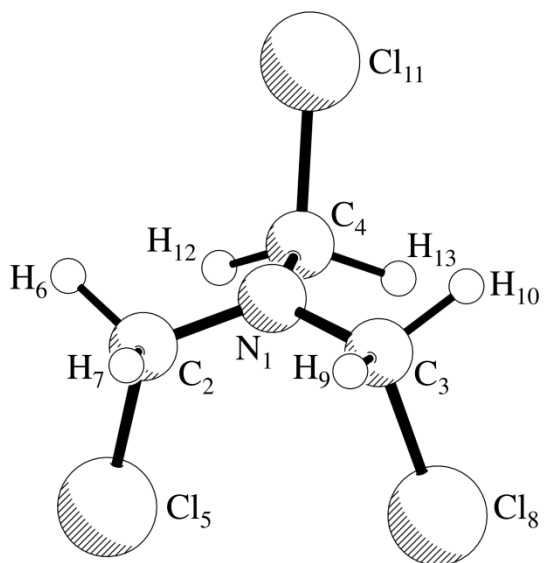

Fig. 1 The lowest-energy ground-state structure of TCMA; the nuclear labelling scheme is outlined.

The highest-level geometry optimizations of TCMA were carried out in the C_s symmetry point group using the SOGGA11-X [45] DFT functional and the cc-pVDZ, cc-pVTZ and cc-pVQZ basis sets [46,47]. Two stationary points were located at this level and the characters of these points were verified using vibrational frequency analysis and confirmed to correspond to minima on the ground-state potential surface. A transition state connecting the two stationary points was located using the synchronous transit-guided quasi-Newton (QST2) approach [48,49] and optimized in the C_1 symmetry point group using the SOGGA11-X DFT functional and the cc-pVDZ, cc-pVTZ, and cc-pVQZ basis sets. The character of the transition state was verified using vibrational frequency analysis.

To establish flexible restraints for use in the SARACEN-type [50-52] GED least-squares refinement procedure, a series of geometry optimizations were carried out in the C_s symmetry point group using the

B3LYP [53,54], B3P86 [53,55], B3PW91 [53,56], and *w*B97XD [57] DFT functionals and employing a scaling range of basis sets of increasing completeness, all belonging to the *def*2 family [58] (*def*2-SVP, *def*2-TZVPP, and *def*2-QZVPP).

The geometry of methenamine ($N_4C_6H_{12}$), a common impurity readily formed on exposure of TCMA to moisture, was optimized in the T_d symmetry point group using the SOGGA11-X DFT functional and the cc-pVDZ, cc-pVTZ, and cc-pVQZ basis sets. A single stationary point was located at this level and the character of this point was verified using vibrational frequency analysis and confirmed to correspond to a minimum on the ground-state potential surface.

Raman frequencies and activities were computed for TCMA and methenamine in the C_s and T_d symmetry point groups, respectively, using the SOGGA11-X DFT functional and the cc-pVTZ basis set.

Where complete basis set (CBS) quality results are referenced (*i.e.* SOGGA11-X/CBS), the property in question has been extrapolated to the CBS limit *via* fitting cc-pVDZ, cc-pVTZ, and cc-pVQZ results with a function of the form:

$$y(x) = y_{CBS} + \beta e^{-\alpha x}, x \in \{2,3,4\}$$

in which y_{CBS} is the value of the extrapolated property, y, at the CBS limit, x takes the values 2, 3 and 4 for cc-pVDZ, cc-pVTZ and cc-pVQZ results, respectively, and α and β are fitting parameters.

An SE-MD simulation was carried out using the PM6 parameterization method [59] in the *NVT* ensemble. The lowest-energy ground-state conformation of TCMA (confirmed *via* theoretical calculations at the SOGGA11-X/cc-pVQZ level) was pre-optimized using the PM6 parameterization method and used as a starting point for the SE-MD simulation. The system was subsequently propagated through time for 0.5 ns using a 1.0 fs time step. The temperature of the system was set to match the average nozzle temperature used in GED data collection (404 K) and was regulated using a chain of five Nosé-Hoover thermostats operating with a wavenumber of 3335 cm^{-1}. A set of single-step distance corrections, amplitudes of vibration and anharmonicity constants was extracted from 0.25 ns of the SE-MD simulation using MD-SIM v0.5.1 [Zakharov, A.V.; personal communication] in accordance with established procedure [60-63].

GED Data Acquisition. GED data for TCMA were acquired using the Edinburgh GED apparatus [64], now housed at the University of Canterbury, NZ. An accelerating potential of 40 keV was applied, producing electrons with an approximate wavelength of 6.0 pm. The scattering intensities were recorded on Kodak Electron Image films at nozzle-to-film distances of 84.5 and 230.0 mm. The sample and nozzle were heated to 351 and 393 K, respectively, for the longer nozzle-to-film distance and to 395 and 413 K, respectively, for the shorter nozzle-to-film distance. A summary of the experimental parameters is tabulated in Table S1.

All GED data were acquired at the University of Edinburgh, UK, and analyzed at the University of York, UK.

GED Data Reduction. An Epson Expression 1680 Pro flat-bed scanner was used to digitize the scattering intensities recorded on the Kodak Electron Image films; digitized diffraction patterns were reduced to

molecular intensity curves (MICs) using an azimuthal averaging routine implemented in the in-house-developed data extraction package *xtract* [Nunes, J. P. F.; personal communication].

Raman Spectroscopy. Raman spectroscopic data for TCMA were acquired using a confocal microscope adapted from a commercially-available inverted fluorescence microscope (Olympus, IX70) and pumped by a 785 nm fiber-coupled diode laser. Volume Bragg-type bandpass filters were used to filter background emission from the pump laser prior to direction of the beam into a 40× microscope objective (NA = 0.65) by a final bandpass filter. Rayleigh and Raman scattered light was collected in a 180° back-scattering geometry through the 40× microscope objective. The scattered light was filtered by three sequential notch filters and focused into a 50 μm optical fiber coupled to a near-IR lens spectrometer (Acton Series LS785, Princeton Instruments) imaged *via* a CCD camera (PIXIS 400, Princeton Instruments). The typical pump power at the sample measured 20 mW. Integration times ranged from 60-300 s. 30 sets of Raman spectroscopic data were acquired in total; 10 at each 293 K, 333 K and 393 K using an in-house-built temperature stage.

All Raman spectroscopic data were acquired at Massey University, NZ, and analyzed at the University of York, UK.

■ RESULTS AND DISCUSSION

Gas-Phase Conformations of Tris(chloromethyl)amine. Our theoretical calculations using the SOGGA11-X DFT functional located two stationary points corresponding to minima on the ground-state potential surface of TCMA; these points are labelled **A** and **B** in Fig. 2. A transition state connecting **A** and **B** (**TS$_{A,B}$**) was located at the same level. Cartesian coordinates and energies from these theoretical calculations using the cc-pVDZ, cc-pVTZ, and cc-pVQZ basis sets are tabulated in Tables S2–S7.

A and **B** are pseudo-rotameric structures that differ primarily in their dihedral angle, dC$_2$–N$_1$–C$_4$–Cl$_{11}$. **A** and **B** formally both belong to the C_s symmetry point group. In **A**, one CH$_2$Cl group is configured synperiplanar to the lone pair on the amine center and two CH$_2$Cl groups are configured antiperiplanar; in **B**, all CH$_2$Cl groups are configured antiperiplanar. Consequently **B** closely resembles the C_s-symmetric 'barstool' structure adopted by TCMA in the single crystal, as determined by Klapötke *et al.* [1] using XRD, but is of higher energy than **A** in the gas phase.

B is evaluated to be 8.9 kJ mol^{-1} higher in energy than **A** at the SOGGA11-X/CBS level. A barrier to interconversion between **A** and **B** of *ca.* 30 kJ mol^{-1} can be estimated from Fig. 2 – direct optimization of **TS$_{A,B}$** gives the most accurate measurement of the barrier to interconversion, which is evaluated to be 29.2 kJ mol^{-1} at the SOGGA11-X/CBS level. The fractional occupation of the potential well containing **B** can consequently be anticipated to be low in the gas phase; applying the Boltzmann distribution equation at the average temperature of the GED experiments (404 K) and using the energy difference evaluated at the SOGGA11-X/CBS level (8.87 kJ mol^{-1}), it is estimated to be approximately 3%. As this is below the sensitivity of the GED technique and, as the barrier to interconversion evaluated at this level is high, **B** was not considered to be present in the GED experiment.
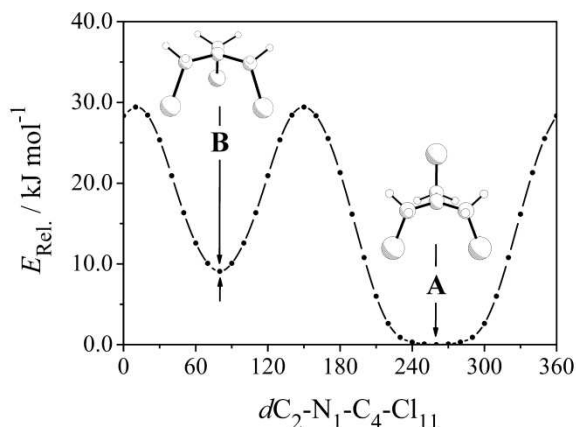
Fig. 2 The relative energy, $E_{\text{Rel.}}$, in kJ mol^{-1} of TCMA as a function of dC$_2$–N$_1$–C$_4$–Cl$_{11}$. The energies are evaluated at the SOGGA11-X/cc-pVQZ level, with full geometry optimization at every point. The stationary points **A** and **B** are indicated.

The least-squares refinement procedure therefore employed a parameterized molecular model describing only **A** in terms of 13 refinable parameters comprising five internuclear distances (p_1-p_5), six angles (p_6-p_{11}), and two dihedral angles (p_{12}-p_{13}). The C_s symmetry of **A** was exploited in order to construct the parameterized molecular model such that it used as few refinable parameters as possible. A description of the parameterized molecular model can be found in the Supporting Information (Eq.S1–S24).

GED Data Analysis. The parameterized molecular model was employed in the ed@ed v3.0 least-squares refinement program [65,66] using the electron scattering factors of Ross *et al.* [67] to conduct a SARACEN-type least-squares refinement. The weighting points for off-diagonal weight matrices, scaling factors and correlation parameters can be found in Table S8. The correlation matrix can be found in Table S9. The least-squares refinement procedure yielded interatomic distances of the $r_{e,\text{MD}}$ type [62], in recognition of the fact that a single-step $r_a - r_e$ correction computed *via* SE-MD simulation was applied.

SARACEN restraints were based on the highest-level SOGGA11-X/cc-pVQZ theoretical parameters and applied to seven of the thirteen refinable parameters. Estimates of the uncertainties related to the SARACEN restraint values were derived from sequential DFT geometry optimizations using the B3LYP, B3P86, B3PW91 and *w*B97XD functionals. Cartesian coordinates and energies from these theoretical calculations using the *def*2-SVP, *def*2-TZVPP, and *def*2-QZVPP basis sets are tabulated in Tables S10–S24. A complete list of the refined and theoretical (SOGGA11-X/cc-pVQZ) parameters with accompanying SARACEN restraints can be found in Table S25.

All amplitudes of vibration associated with a given peak in the radial distribution curve (RDC) were tied using a fixed ratio to the amplitude of vibration associated with the nuclear pair that gave rise to the largest scattering effect under that peak. Only this amplitude of vibration was refined for each peak in the RDC. Of the nine amplitudes of vibration that were refined, four were refined freely while five were restrained. A

complete list of internuclear distances, refined and theoretical amplitudes of vibration and distance corrections can be found in Table S26.

The experimentally-acquired and experimental-minus-theoretical 'difference' MICs are presented in Fig. 3. Fourier transformation of the MIC yields the RDC; an experimentally-acquired and experimental-minus-theoretical 'difference' RDC for **A** is presented in Fig. 4.
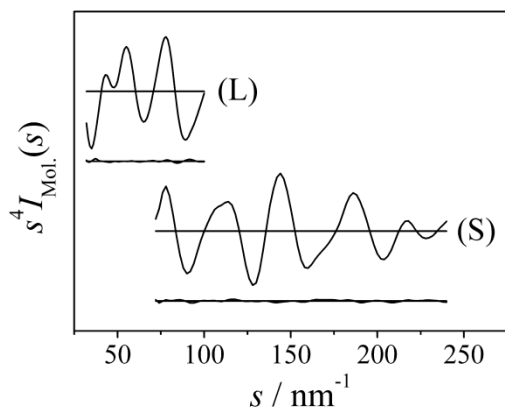

Fig. 3 MICs and experimental-minus-theoretical 'difference' MICs acquired on reduction of long (L) and short (S) GED data acquired for TCMA
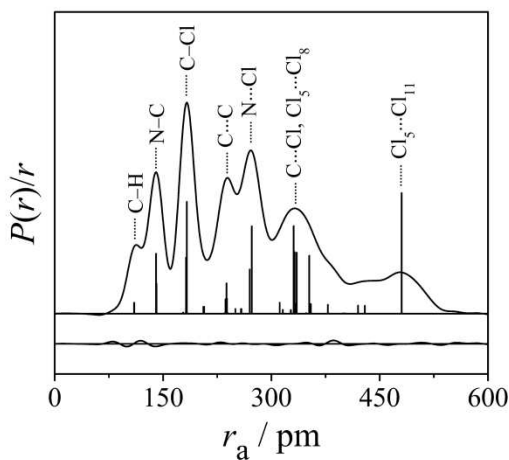
Fig. 4 RDC and experimental-minus-theoretical 'difference' RDC acquired on refinement of GED data acquired for TCMA

The R_G factor obtained for the least-squares refinement of **A** was 0.097 and the R_D factor (which ignores the off-diagonal elements of the weight matrix) was 0.059. Readers unfamiliar with the difference between the R_G and R_D factors may find Ref. 68 instructive. Refined Cartesian coordinates for the experimentally-determined structure of **A** can be found in Table S27. Table 1 contains selected equilibrium structural parameters for **A**.

The structure of **A** is accurately determined using GED, with internuclear distances and angles typically being determined to within an uncertainty of a little over a tenth of a picometer and of a degree, respectively. The agreement between the values of the experimental and theoretical equilibrium structural parameters attests to the acceptable accuracy of the applied theoretical calculations at the SOGGA11-X/cc-pVQZ level and of our GED structural solution. All internuclear distances and angles are determined *via* GED to 1.6(1) pm and 0.62(13)° of the SOGGA11-X/cc-pVQZ results, respectively.

Table 1 A Selection of Important GED ($r_{e,MD}$) and Theoretical (r_e, SOGGA11-X/cc-pVQZ) Equilibrium Structural Parameters[a] for **A**

Parameter(s)	$r_{e,MD}$	r_e
rN$_1$–C$_2$	139.1(2)	140.8
rN$_1$–C$_4$	140.0(2)	141.7
rC$_2$–Cl$_5$	184.1(1)	183.4
rC$_4$–Cl$_{11}$	183.0(2)	182.3
aN$_1$–C$_2$–Cl$_5$	114.14(17)	114.74
aN$_1$–C$_4$–Cl$_{11}$	111.98(21)	112.60
aC$_2$–N$_1$–C$_3$	119.40(20)	120.77
aC$_2$–N$_1$–C$_4$	117.13(17)	118.50

[a] Internuclear distances (r) are tabulated in picometers (pm) and angles (a) are tabulated in degrees. Refer to Fig. 1 for the nuclear labelling scheme.

It is clear on visual inspection of the final single peak in the RDC in Fig. 4 that **A**, in which one CH$_2$Cl group is configured synperiplanar to the lone pair on the amine centre and two CH$_2$Cl groups are configured antiperiplanar, is the structure adopted in the gas phase. Were this not to be the case, the final peak in the RDC {rCl$_5$···Cl$_{11}$, r_a = 481.1(6) pm} would either be shifted to a smaller r_a value, indicative of **B**, or split into two peaks, indicative of an alternative C_1-symmetric structure with one or more CH$_2$Cl groups configured synclinal. Oberhammer *et al.* have previously applied a similar rationale to N(CH$_3$)$_2$(CH$_2$F) [19]. To obtain a measure for the dihedral dC$_2$–N$_1$–C$_4$–Cl$_{11}$, which is characteristic of the configuration adopted, twenty-two least-squares refinements have been carried out with dC$_2$–N$_1$–C$_4$–Cl$_{11}$ set to values greater than and less than that associated with the ideal synperiplanar configuration to give a series of $R_G/R_{G,Min.}$ datapoints, presented in Fig. 5. The 99% confidence limit is indicated.
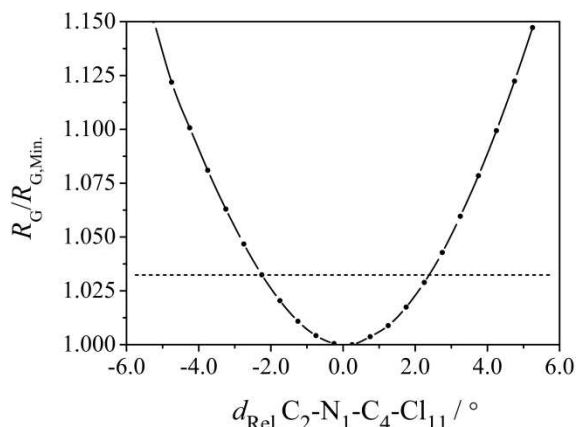
Fig. 5 $R_G/R_{G,Min.}$, indicative of the quality of the least-squares refinement of TCMA, as a function of the relative value of $dC_2–N_1–C_4–Cl_{11}$, dRel.$C_2–N_1–C_4–Cl_{11}$, compared to the ideal synperiplanar configuration of $C_4–Cl_{11}$ with respect to the lone pair on the amine center. The dotted line represents the 99% confidence limit.

The Anomeric Effect in Tris(chloromethyl)amine. It is of particular interest to the structural community to note that all N–C internuclear distances in the experimentally-determined structure of **A** {$rN_1–C_2 = rN_1–C_3 =$ 139.1(2) pm, $rN_1–C_4 =$ 140.0(2) pm} are substantially shorter than the typical N–C(sp^3) internuclear distances found in free molecules of analogous alkylated tertiary amines in the gas phase {$NH_2(CH_3)$, $rN–C(sp^3) =$ 147.2(3) pm [8]; $NH(CH_3)_2$, $rN–C(sp^3) =$ 145.5(2) pm [7]; $N(CH_3)_3$, $rN–C(sp^3) =$ 145.2(2) pm [5]; $NH(CH_2CH_3)_2$, $rN–C(sp^3) =$ 146.0(1) pm [9]; $N(CH_2CH_3)_3$, $rN–C(sp^3) =$ 146.4(1) pm [9]}, indicative of partial double-bond character being associated with these internuclear distances. In contrast, all three C–Cl internuclear distances in the experimentally-determined structure of **A** {$rC_2–Cl_5 = rC_3–Cl_8 =$ 184.1(1) pm, $rC_4–Cl_{11} =$ 183.0(2) pm} are somewhat longer than those calculated for analogous free molecules {$NH_2(CH_2CH_2Cl)$, $rC(sp^3)–Cl =$ 179.6 pm (CCSD/cc-pVTZ) [69]} in the gas phase. This is in harmony with the observations of Klapötke *et al.* [1] for the single crystal, the earlier observations of Oberhammer *et al.* [18-25] made using GED regarding the anomeric effect in $N(CH_3)_2(CH_2F)$ and the theoretical work [26-30] in the literature regarding the anomeric effect in $NH_2(CH_2F)$. A classic 'no-bond-double-bond' [18,19] resonance scheme, invoked to describe the geometric consequences of the anomeric effect in species such as $N(CH_3)_2(CH_2F)$ (measurably shortened and lengthened $rN–C$ and $rC–F$ internuclear distances, respectively, and an increase in the $aN–C–F$ angle [18,19]) can be adapted to give the immonium-like resonance structures of Scheme 1 for **A**, similar to that given by Klapötke *et al.* [1] give for the single crystal.
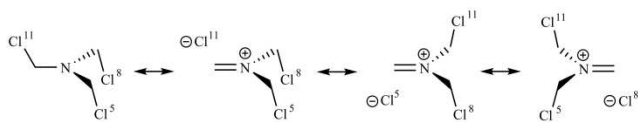
Scheme 1 Classic 'no-bond-double-bond' resonance scheme for **A**. Mesomeric forms of **A** have been rotated to place the double bond in the plane of the page for clarity.

The anomeric effect in a range of fluorinated tertiary amines studied by Oberhammer *et al.* [18-25] stabilizes the antiperiplanar configuration of the C–F bond with respect to the lone pair on the amine centre relative to the synperiplanar configuration, the strength of the stabilization conferred being both proportional to the orbital overlap between the C–F σ^* orbital and the lone-pair-containing orbital on the amine centre and inversely proportional to the energy difference between the two orbitals [18]. Oberhammer *et al.* consequently report observing only the antiperiplanar configuration for species such as $N(CH_3)_2(CH_2F)$ and $N(CH_3)_2(CF_3)$ [18,19] in the gas phase. In the structure of TCMA reported by Klapötke *et al.* [1] for the single crystal, the three C–Cl bonds similarly adopt antiperiplanar configurations with respect to the lone pair on the amine centre. In the gas phase; however, TCMA adopts the structure of **A** in which two CH_2Cl groups are configured antiperiplanar while one is configured synperiplanar. The geometric consequences of the anomeric effect are therefore not uniform for all CH_2Cl groups in TCMA.

In contrast to the structure reported by Klapötke *et al.* [1] for the single cystal, $r N_1$–C_4 is neither shortened nor is $r C_4$–Cl_{11} lengthened – both being associated with the CH_2Cl group that is configured synperiplanar – to more or less the same extent as the other N–C and C–Cl internuclear distances in **A** that are associated with the two CH_2Cl groups that are configured antiperiplanar. $r N_1$–C_4 is determined *via* GED to be 0.9(4) pm longer than $r N_1$–C_2 and $r N_1$–C_3, and $r C_4$–Cl_{11} to be 1.1(3) pm shorter than $r C_2$–Cl_5 and $r C_3$–Cl_8. We note that $r C_2$–Cl_5 and $r C_3$–Cl_8 are lengthened somewhat more than might be expected were all resonance structures of Scheme 1 to be equally weighted.

These observations can be rationalized using molecular orbital theory. For **B**, in which all CH_2Cl groups are configured antiperiplanar, orbital overlap of the C_4–Cl_{11} σ^* orbital with the lone-pair-containing orbital on N is at the most optimal and, furthermore, is more or less equal to the overlap obtained by the other two CH_2Cl groups. This situation is illustrated schematically in Fig. 6. $r N_1$–C_4:$r N_1$–C_2 and $r C_4$–Cl_{11}:$r C_2$–Cl_5 ratios of approximately 1:1 can be expected in this case. For **A**, orbital overlap of the C_4–Cl_{11} σ^* orbital with the lone-pair-containing orbital on N is sub-optimal relative to the overlap obtained by the other two CH_2Cl groups. This situation too is illustrated schematically in Fig. 6. $r N_1$–C_4:$r N_1$–C_2 and $r C_4$–Cl_{11}:$r C_2$–Cl_5 ratios of somewhat more than and less than 1:1 can be expected, respectively, in harmony with a weakened anomeric effect exerted on the synperiplanar CH_2Cl group. These ratios, determined at the SOGGA11-X/cc-pVQZ level, are plot as a function of $d C_2$–N_1–C_4–Cl_{11} in Fig. 6. For **A**, these ratios are 1.007 and 0.994, respectively, and for **B**, these ratios are both 1.000, if they are evaluated at the SOGGA11-X/cc-pVQZ level. It is on this basis that we conclude that the first 'no-bond-double-bond' resonance structure in Scheme 1 should be weighted less heavily than the other two 'no-bond-double-bond' resonance structures for **A**. Inspection of the Mulliken charge distribution in **A** and **B** from our theoretical calculations at the SOGGA11-X/cc-pVQZ level further supports this conclusion as Cl_5, Cl_8 and Cl_{11} share equal Mulliken charges in **B** {$Cl_5 = Cl_8 = Cl_{11} = -0.123$ a.u} and unequal charges in **A** {$Cl_5 = Cl_8 = -0.146$ a.u; $Cl_{11} = -0.138$ a.u}. Although the geometric consequences of electrostatic effects should also in principle be measurable, and are inseparable from those of the anomeric effect, work by Oberhammer *et al.* on $N(CH_3)_2(CH_2F)$ [19] suggests that the influence of the former on internuclear distances is less in magnitude than influence of the latter.
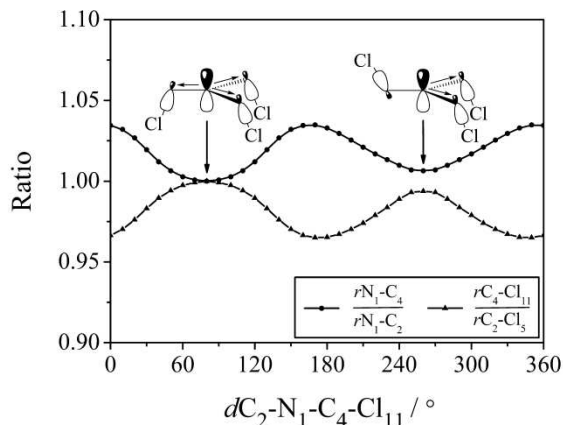
Fig. 6 The ratios rN$_1$–C$_4$:rN$_1$–C$_2$ and rC$_4$–Cl$_{11}$:rC$_2$–Cl$_5$ as a function of dC$_2$–N$_1$–C$_4$–Cl$_{11}$. The ratios are evaluated at the SOGGA11-X/cc-pVQZ level, with full geometry optimization at every point. Schematic orbital overlap diagrams are overlayed. The label on the amide centre is omitted from the orbital overlap diagrams for clarity.

Large aN–C–Cl angles – equally characteristic geometric consequences of the anomeric effect – are also acknowledged in the experimentally-determined structure of **A** {aN$_1$–C$_2$–Cl$_5$ = aN$_1$–C$_3$–Cl$_8$ = 114.14(17)°; aN$_1$–C$_4$–Cl$_{11}$ = 111.98(21)°}. The geometry around all three C nuclei deviates considerably from the ideal tetrahedron. The aN$_1$–C$_4$–Cl$_{11}$ angle deviates less than either the aN$_1$–C$_2$–Cl$_5$ or aN$_1$–C$_3$–Cl$_8$ angles, by only 2.51(21)° compared to 4.67(17)°, however, and measures 2.17(38)° less than the latter two. This point is consistent with our conclusions. These angles are all smaller than those determined by Oberhammer *et al.* for N(CH$_3$)$_2$(CH$_2$F) and N(CH$_3$)$_2$(CF$_3$) [18,19] {N(CH$_3$)$_2$(CH$_2$F) aN–C–F = 115.9(24)° [19]; N(CH$_3$)$_2$(CF$_3$) aN–C–F = 115.1(10)° [19]}, indicative of a predictably weaker anomeric effect in TCMA, yet the geometric consequences are still quite measurable *via* GED, even when experimental uncertainties are taken into account.

The adoption of different structures in the gas phase and in the single crystal could be rationalized on the basis of the net dipole moment of TCMA as a function of dC$_2$–N$_1$–C$_4$–Cl$_{11}$ (Fig. 7). In the single crystal structure, in which the three C–Cl bonds adopt antiperiplanar configurations with respect to the lone pair on N, the net dipole moment of the TCMA molecule is maximized. In the unit cell, molecules of TCMA are predictably aligned antiparallel [1] such that there is consequently no net dipole moment for the single crystal. The net dipole moment is similarly maximized for **B**. The gas-phase structure, **A**, in which two CH$_2$Cl groups are configured antiperiplanar while one is configured synperiplanar, is located in a lower-energy region of the ground-state potential surface where the net dipole moment is at a minimum. The stabilization conferred by the anomeric effect is weakened for **A** relative to **B**, but could be compensated for *via* minimization of the dipole moment.
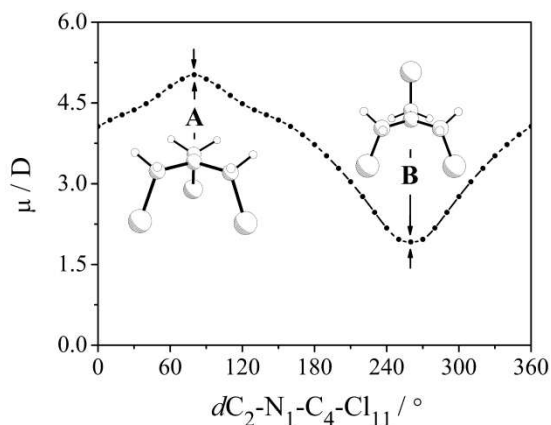
Fig. 7 The net dipole moment, μ, in Debye of TCMA as a function of dC$_2$–N$_1$–C$_4$–Cl$_{11}$. The net dipole moments are evaluated at the SOGGA11-X/cc-pVQZ level, with full geometry optimization at every point. The stationary points **A** and **B** are indicated.

From Scheme 1, the predisposition of TCMA towards substitution at C$_1$, C$_2$ or C$_3$ [1] can be understood, accounting for the sensitivity of TCMA to moisture. Degradation of our sample of TCMA in transit between the sublimation tube and the analytical instruments used in this work spoilt initial batches of product. Methenamine, readily formed on exposure of TCMA to moisture, is difficult to avoid and is the identity of one confirmed impurity remaining in the final production batch; the presence of trace quantities of methenamine has been confirmed *via* Raman spectroscopy.

Raman Spectroscopy of Tris(chloromethyl)amine. The experimental solid-state Raman spectrum of TCMA, recorded at 298 K, is presented in Fig. 8.
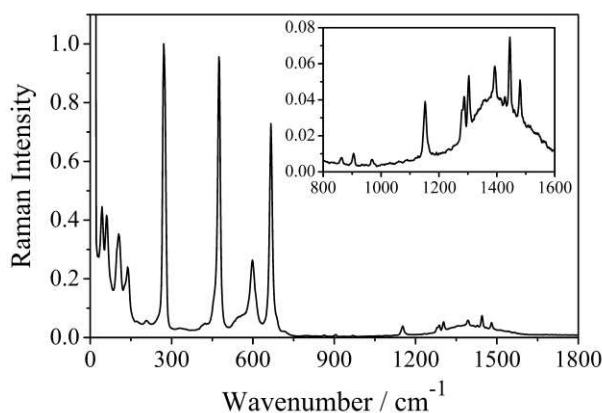

Fig. 8 Experimentally-acquired solid-state Raman spectrum of TCMA recorded at 298 K with expansion of the wavenumber region 800–1600 cm^{-1}

The assignment of Raman-active intramolecular modes was guided by the computation of theoretical wavenumbers and Raman activities at the SOGGA11-X/cc-pVTZ level for **B**. **B** modestly resembles the C_s-symmetric 'barstool' structure of TCMA adopted in the single crystal; no empirical corrections were applied to **B**. The computation of theoretical wavenumbers and Raman activities at the SOGGA11-X/cc-pVTZ level for methenamine was also used to assist the assignment of the Raman spectrum. Although not present in sufficient quantities in the gas phase to be detectable *via* GED, the sensitivity of the Raman spectroscopy technique is such that the presence of methenamine may be confirmed *via* experiment. All assignments of the Raman-active intramolecular modes of **B** are made with modest confidence, with experimental and scaled theoretical Raman band wavenumbers differing by only 13(2) cm^{-1} on average. Although still clearly recognizable as the experimental bands at 599.8 and 666.5 cm^{-1} from their theoretical Raman intensities, the theoretical bands at 651.7 and 714.1 cm^{-1} are furthest from their experimental counterparts; both bands correspond to C–Cl stretching modes, the wavenumber of which is predicted poorly due to non-negligible structural differences between **B**, as determined at the SOGGA11-X/cc-pVTZ level, and the single-crystal structure of TCMA. All other internuclear distances and angles in **B** are determined to 0.3(3) pm and 1.2(4)° of the single-crystal structure, but rC2–Cl5 and rC4–Cl11 are determined to be 2.4(2) pm and 1.8(3) pm shorter, respectively, shifting the theoretical peaks to higher wavenumbers.

Experimental Raman band wavenumbers and indications of the relative intensity of these bands are given in Table 2 alongside their suggested identity; the latter is supported by tabulation of theoretical wavenumbers (both scaled and unscaled) for the suggested Raman-active intramolecular mode. Theoretical Raman activities are also tabulated.

Table 2 A Summary of Experimental Wavenumbers,[a] Relative Intensities[b] and Suggested Assignments[c] Supported by Theoretical[d] (Both Unscaled and Scaled) Wavenumbers, Symmetries and Raman Activities for Raman Bands Observed in Fig. 8

Experimental	Theoretical				
Wavenumber	Wavenumber (unscaled)	Wavenumber (scaled)	Symmetry	Raman Activity	Assignment
43.6(s)					
60.2(s)					Lattice/Intramolecular Modes
104.9(s)					
137.5(s)					
270.9(vs)	274.2	263.0	A'	6.355	scC–C–Cl
	274.7	263.4	A"	6.355	
474.2(vs)	456.6	437.9	A"	1.661	scC–N–C
	456.9	438.2	A'	1.659	
	473.7	454.3	E	2.529	{M} scC–N–C, twCH$_2$
	506.8	486.0	A'	9.771	i, v_sC–Cl
599.8(vs)	679.6	651.7	A'	10.616	v_aC–Cl
	679.8	651.9	A"	10.594	

	695.8	667.3	T2	1.348	{M} scC–N–C, ρC–N–C, ρCH$_2$
664.5(vs)	744.6	714.1	A'	22.536	i, v_sC–Cl
863.2(vw)	869.1	833.5	T2	2.053	{M}: v_sN–C, ρCH$_2$
904.6(vw)	921.9	884.1	A'	0.003	v_sN–C
968.2(vw)	992.5	951.8	A"	0.196	ρCH$_2$
	992.9	952.2	A'	0.198	
1038.9(vw)	1062.0	1018.5	T2	5.072	{M} v_aN–C, ρCH$_2$
1042.3(vw)	1070.9	1027.0	A1	4.487	{M} v_sN–C
1060.9(vw)	1078.1	1033.9	E	2.314	{M} v_aN–C, ρCH$_2$
1152.3(m)	1199.2	1150.0	A'	4.209	v_aN–C, twCH$_2$, ρN–C–H
	1199.3	1150.1	A"	4.200	
1280.0(m)	1295.6	1242.5	T2	3.080	{M} scC–N–C, ρCH$_2$, v_aN–C
1286.4(m)	1334.2	1279.5	A'	5.482	wa_aCH$_2$
	1334.7	1280.0	A"	5.502	
1303.4(m)	1362.7	1306.8	A'	4.550	wa_sCH$_2$
	1436.4	1377.5	A'	3.694	v_aN–C, twCH$_2$, scN–C–H
1393.2(m)	1436.6	1377.7	A"	3.697	
	1421.0	1362.7	T2	0.942	{M} wa_sCH$_2$, v_aN–C
1445.0(m)	1495.6	1434.3	A'	7.612	sc_aCH$_2$
	1495.7	1434.4	A"	7.579	
1480.0(m)	1526.6	1464.0	A'	2.857	sc_sCH$_2$

[a] All wavenumbers, experimental and theoretical, are tabulated in cm^{-1}. [b] vs, very strong; s, strong; m, medium; w, weak; vw, very weak. [c] v, stretching; tw, twisting; wa, wagging; ρ, rocking; sc, scissoring; i, nitrogen inversion/"umbrella". The subscripts 's' and 'a' indicate whether the mode is symmetric or anti-symmetric, respectively. All assignments preceded by {M} refer to Raman-active intramolecular modes of methenamine. [d] Calculations at the SOGGA11-X/cc-pVTZ level. The appropriate scaling factor is 0.959 [70].

Raman bands that are not readily assignable to a Raman-active intramolecular mode of TCMA can be categorized into two sets; those with wavenumbers < ca. 200 cm^{-1} and those with wavenumbers > ca. 400 cm^{-1}. The former manifest strongly in the spectrum and may be attributed to intermolecular/lattice modes; these Raman bands obscure those arising from the antisymmetric rocking ρ_aCH$_2$Cl modes [theoretical wavenumbers: 76.9 and 78.2 cm^{-1} (unscaled); 73.7 and 75.0 cm^{-1} (scaled)] and symmetric rocking ρ_sN–C–Cl mode [theoretical wavenumber: 110.5 cm^{-1} (unscaled); 106.0 cm^{-1} (scaled)] and make the identification of these modes challenging. The latter show only weakly in the spectrum and are attributable to the presence of the trace impurity methenamine. Where a Raman band is assigned to methenamine in Table 2, it is supported by tabulation of theoretical wavenumbers (both scaled and unscaled) for the suggested Raman-active intramolecular mode. For these assignments, experimental and scaled theoretical Raman band wavenumbers differ by 23(2) cm^{-1} on average.

Raman spectra recorded at 298, 333 and 393 K as the sample was heated through the literature melting point (366 K) [40] have allowed us to study the solid and the melt independently. These experimental Raman

spectra, in the wavenumber region 200–1000 cm^{-1}, are presented in Fig. 9 (A-C) alongside theoretical Raman spectra computed at the SOGGA11-X/cc-pVTZ level for **B** (D) and **A** (E).
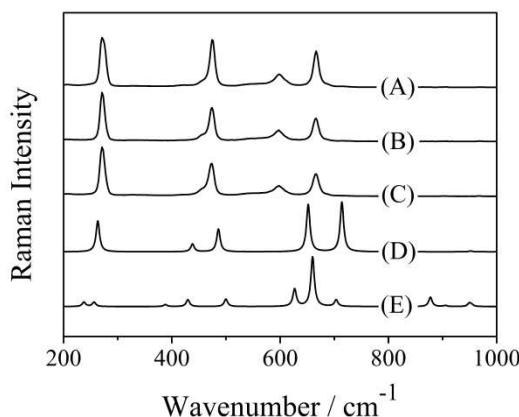

Fig. 9 Experimental solid-state and melt Raman spectra of TCMA in the wavenumber region 200–1000 cm^{-1}, recorded at 298 (A), 333 (B) and 393 K (C); theoretical Raman spectra of **B** (D) and **A** (E) are available for comparison

Raman-active intramolecular modes are observed to thermally broaden slightly but remain otherwise unchanged on transition from the solid state into the melt. The expected spectral changes on transition from **B** to **A**, as predicted *via* theory and illustrated in Fig. 9, are not observed. The three experimental Raman spectra are an acceptable match to the theoretical Raman spectrum of **B**; experimental and theoretical Raman bands differ only by 12(4) cm^{-1} over the wavenumber region 200–1000 cm^{-1}.

It is sensible to conclude that a structure similar to **B**/that of the single crystal in which the three C–Cl bonds adopt antiperiplanar configurations with respect to the lone pair on the amide centre is also adopted in the melt. It is uniquely in the gas phase that, free from intermolecular interaction and without stabilization of the large dipole moment of **B**, it is has so far been possible to observe **A**.

■ ASSOCIATED CONTENT

Supporting Information

Summary of parameters for the GED data collection (Table S1); the Cartesian coordinates and energies of **A** and **B** as optimized at the SOGGA11-X level (Tables S2–S4); the Cartesian coordinates and energies of **TS$_{A,B}$** as optimized at the SOGGA11-X level (Tables S5–S7); summary of parameters for the GED data refinement (Table S8); least-squares correlation matrix for the GED data refinement (Table S9); the Cartesian coordinates and energies of **A** as optimized at the B3LYP (Tables S10–S12), B3P86 (Tables S13–S15), B3PW91 (Tables S16–S18) and *w*B97XD (Tables S19–S21) levels; the Cartesian coordinates and energies of methenamine as optimized at the SOGGA11-X level (Tables S22–S24); details of the molecular model used in the least-squares refinement procedure; refined parameters, and SARACEN restraints (Table S25); interatomic distances, GED-determined and theoretical amplitudes of vibration, and MD-derived distance corrections (Table S26); the refined GED structure of TCMA in Cartesian coordinates (Table S27).

Compliance with Ethical Standards. No human or animal studies were conducted as part of this research.

Conflict of Interest. The authors declare that they have no conflict of interest.

■ REFERENCES

1. Klapötke, TM, Krumm, B, Scherr, M, Steemann, FX, Banert, K, Joo, YH (2009) Experimental and Theoretical Studies on Some Energetic Functionalized Trimethylamine Derivatives. Chem Eur J 15:11341-11345.

2. Livingston, RL, Vaughan, G (1956) The Molecular Structure of Perfluorotrimethylamine by Electron Diffraction. J Am Chem Soc 78:4866-4869.

3. Bürger, H, Niepel, H, Pawelke, G (1979) Vibrational Spectra and Normal Coordinate Analysis of CF$_3$ Compounds: Part XXVII. Perfluorotrimethylamine. Reinvestigation of the Molecular Structure by Electron Diffraction. J Mol Struct 54:159-174.

4. Dimitrov, A, Mack, HG, Rüdiger, S, Seppelt, K, Oberhammer, H (1994) Structure and Conformation of Tris(2,2,2-trifluoroethyl)amine, N(CH$_2$CF$_3$)$_3$, in the Gaseous and Solid State. J Phys Chem A 98:11401-11405.

5. Beagley, B, Medwid, AR (1977) Vibrational Force Fields and Amplitudes and Zero-Point Average Structures of (CH$_3$)$_3$Y Molecules (Y = N, P, As, Sb, Bi): A Combination of Electron-Diffraction and Spectroscopic Data. J Mol Struct 38:229-238.

6. Higginbotham, HK, Bartell, LS (1965) Electron Diffraction Study of CH$_3$NH$_2$ and CD$_3$ND$_2$. J Chem Phys 42:1131-1132.

7. Beagley, B, Hewitt, TG (1968) Electron Diffraction Study of Gaseous Dimethylamine and Trimethylamine. Trans Faraday Soc 64:2561-2570.

8. Iijima, T, Jimbo, H, Taguchi, M (1986) The Molecular Structure of Methylamine in the Vapour Phase. J Mol Struct144:381-383.

9. Takeuchi, H, Kojima, T, Egawa, T, Konaka, S (1992) Molecular Structure and Conformations of Diethylamine and Triethylamine as Determined by Gas Electron Diffraction, Ab Initio Calculations and Vibrational Spectroscopy. J Phys Chem A 96:4389-4396.

10. Nishikawa, T, Itoh, T, Shimoda, K (1955) Molecular Structure of Methylamine from Its Microwave Spectrum, J Chem Phys 23:1735-1736.

11. Lide Jr., DR (1957) Structure of the Methylamine Molecule. I. Microwave Spectrum of CD_3ND_2. J Chem Phys 27:343-352.

12. Lide Jr., D. R (1958) Microwave Spectra of Molecules Exhibiting Internal Rotation. III. Trimethylamine. J Chem Phys 28:572-576.

13. Kumar, K (1971) Rotational Isomerism in Triethylamine. Chem Phys Lett 9:504-507.

14. Crocker, C, Goggin, PL (1978) Infrared and Raman Spectroscopic Studies of Conformations in Liquid and Solid Triethyl-, Diethyl(methyl)- and Ethyldimethyl- Amines, -Phosphines and -Arsines. J Chem Soc Dalton Trans 388-394.

15. Bushweller, CH, Fleischman, SH, Grady, GL, McGoff, P, Rithner, CD, Whalon, MR, Brennan, JG, Marcantonio, RP, Dominigue, RP (1982) Stereodynamics of Diethylmethylamine and Triethylamine. J Am Chem Soc 104:6224-6236.

16. Lemieux, RU (1971) Newer Developments in the Conformational Analysis of Carbohydrates. Pure Appl Chem 27:527-548.

17. Edward, JT (1955) Stability of Glycosides to Acid Hydrolysis. Chem Ind 1102-1104.

18. Oberhammer, H (2006) Anomeric Effect in the N-C-F Moiety. Mendeleev Commun 16:136-137.

19. Christen, D, Mack, HG, Rüdiger, S, Oberhammer, H (1996) The Anomeric Effect in (Fluoromethyl)dimethylamine, $CH_2FN(CH_3)_2$. J Am Chem Soc 118:3720-3723.

20. Jin, AD, Zhu, XL, Kirchmeier, RL, Shreeve, JM, Patel, NR, Oberhammer, H (1994) The Effect of Fluorination in Trimethylamine – Gas-Phase Structures of $CF_3N(CH_3)_2$ and $(CF_3)_2NCH_3$. J Mol Struct 323:129-134.

21. Minkwitz, R, Lamek, D, Korn, M, Oberhammer, H (1993) On the Gas Phase Structure of CF3NCl2 and the Preparation of $CF_3NCl_2F^+MF_6^-$ (M = As, Sb) and $CF_2=NClF^+SbF_6^-$. Anorg Allg Chem 619:2066-2070.

22. Minkwitz, R, Lamek, D, Korn, M, Oberhammer, H (1994) The Gas Phase Structure of CF_3NBr_2 and $(CF_3)_2NBr$. Anorg Allg Chem 620:353-356.

23. Bürger, H, Pawelke, G, Oberhammer, H (1982) Vibrational Spectra and Normal Coordinate Analysis of CF3 Compounds Part XLI. Vibrational Spectra, Normal Coordinate Analysis and Electron Diffraction Investigation of Hexafluoroazomethane and *cis*- and *trans*-1,1,1,4,4,4-Hexafluorobut-2-ene. J Mol Struct 84:49-68.

24. Bürger, H, Pawelke, G, Oberhammer, H (1985) Vibrational Spectra and Normal Coordinate Analysis of CF3 Compounds Part XLVI. Synthesis, Vibrational Spectra, Normal Coordinate Analysis and Electron Diffraction Investigation of the *cis* Isomer of Hexafluoroazomethane. J Mol Struct 128:283-295.

25. Dorofeeva, OV, Mitin, AV, Altova, EP, Karasev, NM, Nabiev, OG, Vilkov, LV, Oberhammer, H (2011) Anomeric Effect in *N*-Aziomethylpyrrolidine: Gas-Phase Electron Diffraction and Theoretical Study. Phys Chem Chem Phys 13:1490-1498.

26. Radom, L, Hehre, WJ, Pople, JA (1972) Molecular Orbital Theory of the Electronic Structure of Organic Compounds XIII. Fourier Component Analysis of Internal Rotation Potential Functions in Saturated Molecules. J Am Chem Soc 94:2371-2381.

27. Schleyer, PvR, Kos, AJ (1983) The Importance of Negative (Anionic) Hyperconjugation. Tetrahedron 39:1141-1150.

28. Schleyer, PvR, Jemmis, ED, Spitznagel, GW (1985) Do Anomeric Effects Involving the Second-Row Substituents, Chlorine, Mercapto and Phosphino Exist? Stabilization Energies and Structural Preferences. J Am Chem Soc 107:6393-6394.

29. Reed, AE, Schleyer, PvR (1988) The Anomeric Effect with Central Atoms Other Than Carbon: Strong Interactions Between Nonbonded Substituents in Mono- and Polyfluorinated First and Second-Row Amines. Inorg Chem 27:3969-3987.

30. Rastelli, A, Cocchi, M (1991) Model Calculations of Chemical Interactions Part 3: Rotational Energy Profiles in Simple Molecules: Evaluation, Additivity and Role of Bond-Bond, Bond-Lone-Pair and Lone-Pair-Lone-Pair Interactions. J. Chem. Soc. Faraday Trans 87:249-258.

31. Szinicz, L. (2005) History of Chemical and Biological Warfare Agents. Toxicology 214:167-181.

32. Fraga, CG, Bronk, K, Dockendorff, BP, Heredia-Langner, A (2016) Organic Chemical Attribution Signatures for the Sourcing of a Mustard Agent and Its Starting Materials. Anal Chem 88:5406-5413.

33. Centers for Disease Control and Prevention. Facts About Nitrogen Mustards. https://emergency.cdc.gov/agent/nitrogenmustard/basics/facts.asp. Accessed 30 Oct 2016

34. Organization for the Prohibition of Chemical Weapons. Annex of Chemicals. https://www.opcw.org/chemical-weapons-convention/annexes/annex-on-chemicals. Accessed 30 Oct 2016

35. Mitzel, NW, Brown, DH, Parsons, S, Brain, PT, Pulham, CR, Rankin, DWH (1998) Differences Between Gas-Phase and Solid-State Molecular Structures of the Simplest Phosphonium Ylide, $Me_3P=CH_2$. Angew Chem Int Ed 37:1670–1672.

36. Mitzel, NW, Lustig, C, Berger, RJF, Runeberg, N (2002) Luminescence Phenomena and Solid-State Structures of Trimethyl and Triethylgallium. Angew Chem Int Ed 41:2519–2522.

37. Mitzel, NW, Vojinovic, K, Foerster, T, Robertson, HE, Borisenko, KB, Rankin, DWH (2005) (Dimethylaminomethyl)trifluorosilane, Me2NCH2SiF3 – A Model for the α-Effect in Aminomethylsilanes. Chem Eur J 11:5114-5125.

38. Hagemann, M, Mix, A, Berger, RJF, Pape, T, Mitzel, NW (2008) Strong Intramolecular Si-N Interactions in the Chlorosilanes Cl3-nHnSi)CH2CH2NMe2 (*n* = 1-3). Inorg. Chem. 47:10554-10564.

39. Hagemann, M, Berger, RJF, Hayes, SA, Stammler, HG, Mitzel, NW (2008) N,N-Dimethylaminopropylsilane: A Case Study on the Nature of Weak Intramolecular Si⋯N Interactions. Chem Eur J 14:11027-11038.

40. Fluck, E, Meiser, P (1971) Preparation of Tris(chloromethyl)amine, $N(CH_2Cl)_3$. Angew Chem Int Ed Engl 10:653.

41. Frisch, MJ, Trucks, GW, Schlegel, HB, Scuseria, GE, Robb, MA, Cheeseman, JR, Scalmani, G, Barone, V, Mennucci, B, Petersson, GA, Nakatsuji, H, Caricato, M, Li, X, Hratchian, HP, Izmaylov, AF, Bloino, J, Zheng, G, Sonnenberg, JL, Hada, M, Ehara, M, Toyota, K, Fukuda, R, Hasegawa, J, Ishida, M, Nakajima, T, Honda, Y, Kitao, O, Nakai, H, Vreven, T, Montgomery Jr., JA, Peralta, JE, Ogliaro, F, Bearpark, M, Heyd, JJ, Brothers, E, Kudin, KN, Staroverov, VN, Kobayashi, R, Normand, J, Raghavachari, K, Rendell, A, Burant, JC, Iyengar, SS, Tomasi, J, Cossi, M, Rega, N, Millam, JM, Klene, M, Knox, JE, Cross, JB, Bakken, V, Adamo, C, Jaramillo, J, Gomperts, R, Stratmann, RE, Yazyev, O, Austin, AJ, Cammi, R, Pomelli, C, Ochterski, JW, Martin, RL, Morokuma, K, Zakrzewski, VG, Voth, GA, Salvador, P, Dannenberg, JJ, Dapprich, S, Daniels, AD, Farkas, Ö, Foresman, JB, Ortiz, JV, Cioslowski, J, Fox, DJ (2009) Gaussian 09 Revision D.01. Gaussian Inc., Wallingford CT.

42. CP2K Developers' Group (2015) CP2K v.3.0.

43. York Advanced Research Computing Cluster. http://www.york.ac.uk/it-services/services/yarcc/.

44. EPSRC National Service for Computational Chemistry Software. http://www.nsccs.ac.uk/.

45. Peverati, R, Truhlar, DG (2011) A Global Hybrid Generalized Gradient Approximation to the Exchange-Correlation Functional That Satisfies the Second-Order Density-Gradient Constraint and has Broad Applicability in Chemistry. J Chem Phys 135:191102.

46. Dunning Jr, TH (1989) Gaussian Basis Sets for Use in Correlated Molecular Calculations I. The Atoms Boron Through Neon and Hydrogen. J Chem Phys 90:1007-1023.

47. Woon, DE, Dunning Jr, TH (1993) Gaussian Basis Sets for Use in Correlated Molecular Calculations III. The Atoms Aluminium Through Argon. J Chem Phys 98:1358-1371.

48. Peng, C, Schlegel, HB (1993) Combining Synchronous Transit and Quasi-Newton Methods for Finding Transition States. Israel J Chem 33:449-454.

49. Peng, C, Ayala, PY, Schlegel, HB, Frisch, MJ (1996) Using Redundant Internal Coordinates to Optimize Equilibrium Geometries and Transition States. J Comp Chem 17:49-56.

50. Mitzel, NW, Smart, BA, Blake, AJ, Robertson, HE, Rankin, DWH (1996) Conformational Analysis of 1,4-Disilabutane and 1,5-Disilapentane by Combined Application of Gas-Phase Electron Diffraction and *Ab Initio* Calculations and the Crystal Structure of 1,5-Disilapentane at Low Temperatures. J Phys Chem A 100:9339-9347.

51. Blake, AJ, Brain, PT, McNab, H, Miller, J, Morrison; CA, Parsons, S, Rankin, DWH, Robertson, HE, Smart, BA (1996) Structure Analysis Restrained by *Ab Initio* Calculations: The Molecular Structure of 2,5-Dichloropyrimidine in Gaseous and Crystalline Phases. J Phys Chem A 100:12280-12287.

52. Mitzel, NW, Rankin, DWH (2003) SARACEN – Molecular Structures from Theory and Experiment: The Best of Both Worlds. Dalton Trans 3650-3662.

53. Becke, AD (1993) Density-Functional Thermochemistry. III. The Role of Exact Exchange. J Chem Phys 98:5648-5652.

54. Lee, C, Yang, W, Parr, RG (1988) Development of the Colle-Salvetti Correlation Energy Formula into a Functional of the Electron Density. Phys Rev B 37:785–789.

55. Perdew, JP (1986) Density-Functional Approximation for the Correlation Energy of the Inhomogeneous Electron Gas. Phys Rev B 33:8822-8824.

56. Perdew, JP, Chevary, JA, Vosko, SH, Jackson, KA, Pederson, MR, Singh, DJ, Fiolhais, C (1992) Atoms, Molecules Solids and Surfaces Applications of the Generalized Gradient Approximation for Exchange and Correlation. Phys Rev B 46:6671–6687.

57. Chai, JD, Head-Gordon, M (2008) Long-Range Corrected Hybrid Density Functionals with Damped Atom-Atom Dispersion Corrections. Phys Chem Chem Phys 10:6615-6620.

58. Weigend, F, Ahlrichs R (2005) Balanced Basis Sets of Split Valence, Triple Zeta Valence and Quadruple Zeta Valence Quality for H to Rn: Design and Assessment of Accuracy. Phys Chem Chem Phys 7:3297-3305.

59. Stewart, JJP (2007) Optimization of Parameters for Semiempirical Methods V: Modification of NDDO Approximations and Application to 70 Elements. J Mol Model 13:1173-1213.

60. Wann, DA, Less, RJ, Rataboul, F, McCaffrey, PD, Reilly, AM, Robertson, HE, Lickiss, PD, Rankin, DWH (2008) Accurate Gas-Phase Experimental Structures of Octasilsesquioxanes ($Si_8O_{12}X_8$; X = H, Me). Organometallics 27:4183-4187.

61. Wann, DA, Reilly, AM, Rataboul F, Lickiss, PD, Rankin, DWH (2009) The Gas-Phase Structure of the Hexasilsesquioxane $Si_6O_9(OSiMe_3)_6$. Z Naturforsch 64:1269-1275.

62. Wann, DA, Zakharov, AV, Reilly, AM, McCaffrey, PD, Rankin, DWH (2009) Experimental Equilibrium Structures: Application of Molecular Dynamics Simulations to Vibrational Corrections for Gas Electron Diffraction. J Phys Chem A 113:9511-9520.

63. Wann, DA, Dickson, CN, Lickiss, PD, Robertson, HE, Rankin, DWH (2011) The Gas-Phase Equilibrium Structures of $Si_8O_{12}(OSiMe_3)_8$ and $Si_8O_{12}(CHCH_2)_8$. Inorg Chem 50:2988-2994.

64. Huntley, CM, Laurenson, GS, Rankin, DWH (1980) Gas-Phase Molecular Structure of Bis(difluorophosphino)amine, Determined by Electron Diffraction. J Chem Soc Dalton Trans 954-957.

65. Fleischer. H, Wann, DA, Hinchley, SL, Borisenko, KR, Lewis, JR, Mawhorter, RJ, Robertson, HE, Rankin, DWH (2005) Molecular Structures of $Se(SCH_3)_2$ and $Te(SCH_3)_2$ using Gas-Phase Electron Diffraction and *Ab Initio* and DFT Geometry Optimisations. Dalton Trans 3221-3228.

66. Hinchley, SL, Robertson, HE, Borisenko, KR, Turner, AR, Johnston, BF, Rankin, DWH (2004) Ahmadian, M.; Jones, J. N.; Cowley, A. H. The Molecular Structure of Tetra-*tert*-butyldiphosphine: An Extremely Distorted, Sterically Crowded Molecule. Dalton Trans 2469-2476.

67. Ross, AW, Fink, M, Hilderbrandt, R (1992) International Tables for Crystallography. Kluwer Academic Publishers, Dordrecht, Netherlands.

68. Masters, SL, Atkinson, SJ, Hölbling, M, Hassler, K (2013) Gas-Phase Molecular Structure of 1,1,1,2-tetrabromo-2,2-dimethyldisilane: Theoretical and Experimental Investigation of a Super-Halogenated Disilane and Computational Investigation of the F, Cl and I Analogues. Struct Chem 24:1201-1206.

69. Møllendal, H, Samdal, S, Guillemin, J (2011) Microwave Spectrum, Conformational Composition and Intermolecular Hydrogen Bonding of (2-Chloroethyl)amine ($ClCH_2CH_2NH_2$). J Phys Chem A 115:4334-4341.

70. Alecu, IM, Zheng, J, Zhao, Y, Truhlar, DG (2010) Computational Thermochemistry: Scale Factor Databases and Scale Factors for Vibrational Frequencies Obtained From Electronic Model Chemistries. J Chem Theory Comput 6:2872-2887.